


Stability of a horizontal vortex in weakly stratified flow

John P. McHugh 

Department of Mechanical Engineering, University of New Hampshire, Durham, New Hampshire 03824, USA

 (Received 26 January 2021; accepted 29 September 2021; published 19 October 2021)

A trailing vortex behind a wing moving through a stratified fluid will act to twist the density field into a pattern where the density profile continuously overturns along the axis of the vortex. This configuration is approximated here with a density field that is overturning periodically along the axis of the vortex. The matching velocity field is found approximately assuming weak stratification and constant axial vorticity at leading order and confining the flow to a fixed radius. This base flow is shown to be unstable to a wave triad consisting of two disturbance waves and a component of the base flow as the third “wave.” Three components of this base flow lead to instability: (1) the twirling component, (2) the streaming component, and (3) the rolling component. All three instabilities depend strongly on the axial length for the density field to overturn (the pitch). The twirling and rolling instabilities are important when the pitch is small and they also depend on the Froude number. The streaming instability is dominant when the pitch is large and is independent of the Froude number.

DOI: [10.1103/PhysRevFluids.6.104802](https://doi.org/10.1103/PhysRevFluids.6.104802)

I. INTRODUCTION

A pair of counterrotating horizontal vortices released in a stratified fluid is an important and relatively simple model of the wake of an airplane. Numerical simulations of this flow with the buoyancy frequency N initially constant have been considered previously by many authors [1–6]. Most of the previous simulations were two dimensional [1–3,5,6]; however, Nomura *et al.* [4] treated a three-dimensional case. Nomura *et al.* [4] chose the initial flow and density profile to be the same for all axial positions. This caused the initially flat horizontal density surface to overturn uniformly along the axial coordinate, similar to the two-dimensional cases.

However, this axially uniform configuration does not match the density field behind lifting surfaces in a stratified fluid. For flow past a lifting surface, such as the wing of an airplane, the undisturbed flat horizontal surface of constant density upstream of the wing gets twisted by the trailing vortex system of the wing. The density profile overturns along the axis of each vortex. This three-dimensional density field cannot be reduced to a two-dimensional case and is distinct from the three-dimensional case of Nomura *et al.* [4]. The configuration treated here is an idealization of this downstream overturning, assuming steady flow and periodicity along the axis of the vortex. This configuration is arguably a closer approximation to stratified flow behind wings than previous models.

The previous numerical simulations have shown that the results depend on the Froude number, often defined for a vortex pair as

$$\tilde{Fr} = \frac{W_0}{b_0 N}, \quad (1)$$

where W_0 is the velocity that one vortex induces at the center of the other vortex and b_0 is the spacing of the vortices. The tilde has been added to distinguish this Froude number from a different definition

of Froude number to be introduced later. Garten *et al.* [1] performed two-dimensional simulations and report that $\tilde{Fr} = 1$ is a transitional value, and with $\tilde{Fr} > 1$ the vortices remain coherent and the vortex pair self-induces vertical propagation. However, with $\tilde{Fr} < 1$ the vortex pair collapses and creates a pattern of internal waves. Once the coherency of the vortices is lost, the vertical motion of the vortex pair also does not happen. Shaw and McHugh [7] treat this same transition with a distributed vortex pair. The vorticity was distributed uniformly over each half of a horizontal line, with opposite sign for opposite sides as with a traditional vortex pair. They used two-dimensional numerical simulations and showed that the distributed vortex also collapses into internal waves at small \tilde{Fr} , although the transitional Froude number was found to be somewhat larger and the resulting flow patterns are different. Furthermore, Shaw and McHugh [7] found that the transition between the two types of behavior appeared to be gradual, rather than a sharp change in behavior normally associated with an instability.

Sarpkaya [8] performed laboratory experiments on the wake of a wing in stratified flow. The wing was towed through a motionless stratified liquid and would be expected to have a density field similar to real-world configurations. Sarpkaya found that for most runs with large values of \tilde{Fr} (Sarpkaya used N^* , which is the inverse of \tilde{Fr}), the Crow instability [9] appeared in the wake. However, for small \tilde{Fr} , the Crow instability does not appear and instead the vortices “continued to spin sometimes in highly disorganized forms along their length”. Sarpkaya also reported that this disorganized behavior sometimes appears in the wake when the value of \tilde{Fr} is large. Thus the simulations of Garten *et al.* [1] and the experiments of Sarpkaya [8] agree that there is a strong Froude number dependence on the behavior of a vortex pair in stratified flow. It will be shown here that the axial length for the density field to overturn (the pitch) is also an important parameter.

The Crow instability [9] is a long-wave instability that causes a vortex pair to ultimately merge and form vortex rings, sometimes visible in airplane contrails. Crow [9] ignored stratification and modeled the wake of an airplane as a pair of irrotational vortices in constant-density flow. The vortices had a finite-size core that he treated with the cutoff method. Crow showed that the dominant effect leading to instability is that each vortex creates a straining field at the location of the other vortex. Crow assumed that the position of the disturbed vortex filament had small slope, restricting the results to long modes. Moore and Saffman [10,11] extended the results by treating a single vortex in constant-density flow and provided an analytical estimate for the growth rate of the long-wave unstable modes. The presence of the second vortex was modeled by imposing a weak strain field. This straining field was uniform along the axis of the vortex. Moore and Saffman modeled the base flow as irrotational outside of a core diameter and uniform axial vorticity inside the core, now known as a Rankine vortex.

Widnall *et al.* [12] showed that there is a short-wave instability in a vortex ring in constant-density flow. Moore and Saffman [13] and Tsai and Widnall [14] treated this short-wave instability, again using a single Rankine vortex in an imposed strain field. The instability of a strained vortex is now known as the elliptical instability, as reviewed by Kerswell [15], and is important in many other flows. There are three components of the base flow treated here that lead to instability and one of them is an elliptic type of instability. The elliptic distortion here is caused by overturning stratification, rather than by the presence of a second vortex, and is not uniform along the axis of the vortex. Furthermore, although the axial vorticity at leading order is chosen to be constant, the velocity field is corrected for weak stratification and the corrected axial vorticity is not constant.

The nonzero axial velocity in the vortex treated below makes the flow similar to a jet with swirl. The stability of an inviscid circular jet with swirl in constant density flow was treated by Lessen *et al.* [16] and Loiseleux *et al.* [17]. Lacaze *et al.* [18] added weak elliptical distortion to the configuration. For all these cases, the axial flow was constant inside the jet and the swirl (azimuthal) velocity had constant vorticity inside the jet and was irrotational outside. The results show that there is an unstable Kelvin-Helmholtz mode due to the jump discontinuity in axial velocity at the edge of the jet, along with an infinite set of neutral helical modes. The vortex treated here is similar, but here the exterior flow is ignored and a rigid cylindrical boundary is imposed. The rigid boundary is used so

that the density field will be axially periodic. The rigid boundary eliminates the Kelvin-Helmholtz mode, but allows the helical modes to exist in approximately the same manner.

Eloy and Le Dizès [19] and Sipp and Jacquin [20] treat the stability of a Lamb-Oseen vortex (also known as a Gaussian vortex) with elliptical distortion. A significant complexity with Lamb-Oseen vortices is that a critical layer may exist. A critical layer in a vortex is a radial position where the azimuthal velocity is equal to the disturbance wave speed. Le Dizès and Laporte [21] treat the stability of Lamb-Oseen vortex pairs, including corotating and counterrotating vortices, as well as vortex pairs that are not equal in strength and size. Critical layers do not exist in vortices with constant axial vorticity, such as Rankine vortices. Here the axial vorticity at leading order is constant, as in a Rankine vortex. Thus the complexity of critical layers is avoided in the present configuration.

The stability of a pair of Lamb-Oseen vortices in stratified flow was recently treated by Ortiz *et al.* [22] assuming a quasisteady base flow. The base flow was determined with two-dimensional numerical simulations. The disturbances were three dimensional. They concluded that the dominant instabilities are again the long-wave Crow instability and the short-wave elliptic instability. They also concluded that stratification is not important for these instabilities for large values of Fr . However, the density of the base flow in the work of Ortiz *et al.* was uniform along the axis of the vortex and thus does not match the flow behind lifting surfaces as well as the present configuration. The instability was caused by the presence of the other vortex, distorting the vortex uniformly along its axis. In contrast, the base flow here has the density overturning downstream, and the stratification is critically important to the instability.

Other instabilities exist and may be important in the vortex wake of an airplane. One case is the centrifugal instability [23], such as that which exists between concentric cylinders and creates Taylor vortices. For the present case, the circulation increases with radial position and centrifugal effects are stable. Another case is the zigzag instability [24,25]. The zigzag instability occurs when the axial alignment of a pair of vortices is disturbed and the direction of propagation of the vortex pair varies along the axis. The present results treat a single vortex, where the zigzag instability does not exist. It is unclear what role the zigzag instability may play in airplane wakes. Finally, the results given here assume weak stratification. There may be other instabilities that appear in overturning flows with strong stratification that have not yet been identified.

The stability results given below treat a stratified steady horizontal isolated vortex with the density field overturning along the axis of the vortex. This configuration is still idealized, but is a closer approximation to the flow behind a wing in the real world and in the laboratory experiments of Sarpkaya [8]. Inviscid incompressible flow with weak stratification is assumed. The rigid boundary condition is imposed at a fixed radius R so that a base density field that is periodic along the axis of the vortex may be easily defined. The base velocity field that matches this density field is determined approximately, assuming constant axial vorticity at leading order. This velocity field is similar to the isolated Rankine vortex treated by previous authors, except here the exterior flow is ignored and the total axial vorticity is not constant.

The disturbances for the instability treated here are pairs of helical waves that form a resonant triad with the base flow, similar to those of Moore and Saffman [10] and subsequent authors. The helical waves are identical to inertial waves in a spinning cylinder with axial periodicity. These inertial waves were discussed by Greenspan [26] and Saffman [27] and were first discovered by Lord Kelvin [28]. There are resonant axial wave numbers where inviscid theory predicts that the inertial waves have unbounded amplitude, as found by Lord Kelvin. An analogous effect occurs in the base flow velocity field given below at isolated parameter values, when the base flow mimics a resonant disturbance wave.

Forced inertial waves in a spinning container of fluid have also been treated previously [29–32]. When the forcing frequency matches one of the resonant frequencies, the behavior is particularly complex [32]. One method of forcing that has received special scrutiny is a precessing spinning cylinder [30]. This configuration has many practical applications, including rotating fluid-filled spacecraft and projectiles [29,30]. The instability that arises in a precessing spinning cylinder has azimuthal component $m = 1$ [30], as with the streaming instability discussed here. The stability

analysis of Lagrange *et al.* [30] is very similar to the present work with $m = 1$. A primary difference is that the work of Lagrange *et al.* includes rigid boundaries at the ends of the cylinder, while here the ends are periodic. Despite this and other differences, the stability results of Lagrange *et al.* show trends that are similar to those of the streaming instability discussed here.

Overturning of a stratified flow also occurs in other flows, such as an unstable stratified shear layer [33,34]. An unstable stratified shear layer will evolve into a pattern of billows, which are a sequence of corotating vortices (rather than counterrotating vortices in the trailing vortex system of a wing). The flow within the billows becomes increasingly complex, with strong mixing and turbulence. The evolution is greatly influenced by the density overturning aspect of the flow. Recently, Mashayek *et al.* [35] treated the importance of overturns by calculating the evolution of several length scales using results from direct numerical simulations. They concluded that for weakly stratified cases, turbulence and mixing are dominated by large density overturns. However, the initial instability is driven by the shear, while the density is initially a stabilizing effect. Only after the flow becomes complex do overturns become important. Furthermore, the initial density field of an unstable shear layer is independent of the coordinate along the billow and the initial overturning is two dimensional. In the configuration treated here the base-state density field overturns in the axial direction and includes positions with statically stable and unstable density profiles. The disturbances can extend over both regions, which then simultaneously influence the stability. In contrast, the density field for the previous results with a stratified shear flow initially are statically stable everywhere. Thus the results here treat a different configuration.

Some instabilities treated below depend on the Froude number Fr , now defined as

$$Fr^2 = \frac{V^2}{Rg},$$

where V is the azimuthal vortex velocity and R is the vortex radius. In contrast to previous studies, the results here also depend on the pitch L , which is the horizontal length for one complete rotation of the density profile. The pitch is accounted for with the parameter k ,

$$k = \frac{2\pi R}{L}.$$

The base flow density field here is chosen to be overturning in the axial direction with the azimuthal component $m = 1$. The matching base flow velocity field is found assuming weak stratification. At the leading order, the velocity is chosen to be axially uniform and have constant axial vorticity, similar to a Rankine vortex. However, the first-order correction to the velocity must conform to the density field and is axially nonuniform and the axial vorticity is not constant. This velocity field has azimuthal components $m = 0, 1, 2$ at first order. Instabilities arise when disturbances interact with each of these base flow components. The $m = 0$ part of the base flow is an axisymmetric flow with swirl that oscillates periodically along the axis and will be called the twirling component. This twirling component is unstable when the base flow pitch is relatively short.

The instability with $m = 1$ will be called the streaming instability, since the flow is primarily a pair of helical streams. Previous work on a precessing cylinder of fluid also found an instability with $m = 1$ [30], as discussed above. Furthermore, Hattori and Fukumoto [36], and the references therein, found an $m = 1$ instability in a helical shaped vortex and referred to it as the curvature instability. This instability is distinct from the streaming instability treated here, since the boundary of the vortex here is straight rather than helical. However, the streaming instability results here are similar to the curvature instability results of Hattori and Fukumoto, showing similar trends. This streaming instability depends strongly on the pitch, becoming increasingly stronger as the pitch becomes large. Surprisingly, this streaming instability is independent of the Froude number.

The $m = 2$ instability will be called the rolling instability, since the base flow motion of this mode has primarily a planar rolling character. Many previous investigations have found an $m = 2$ instability in an inviscid vortex, starting with those of Moore and Saffman [10,11,13] and Tsai and

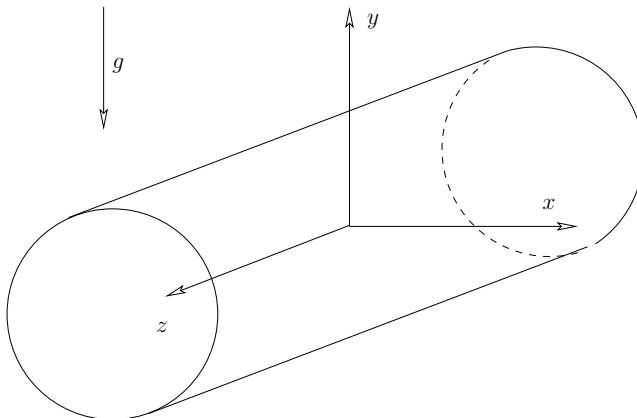


FIG. 1. Schematic diagram of the geometry.

Widnall [14]. The $m = 2$ instability is an elliptic-type instability and is the result of the distortion of streamlines [15]. The rolling instability also depends strongly on the pitch and is the dominant instability when pitch is small.

The unstable twirling modes ($m = 0$) and rolling modes ($m = 2$) found here have disturbances with growth rates that are inversely proportional to the square of the Froude number. Thus large Froude numbers are not stable, but the instability is weaker and thus likely to be overcome by the addition of viscosity and dissipation.

Section II discusses the base-state flow for the overturning stratified vortex. Section III discusses the stability analysis. Section IV presents the results. Section V summarizes.

II. STEADY STRATIFIED VORTEX

A. Base-state density field

The base state is a steady overturning stratified flow. The geometry and coordinate system is shown schematically in Fig. 1. Rather than the typical background vertical density profile, the approach here will treat a flow with a background spiral density pattern. An isolated vortex in an unbounded fluid is of primary interest; however, here an outer boundary consisting of a rigid cylinder is included so that the density field may be easily defined to be axially periodic.

A spiral density field is defined starting with a density profile that is linearly decreasing with altitude,

$$\rho = \rho_0 - By',$$

where ρ_0 and B are constant and y' is a coordinate in the plane perpendicular to the axis of the vortex. Now rotate this profile uniformly about the z axis by transforming the coordinates using

$$x' = x \cos \phi + y \sin \phi, \quad y' = -x \sin \phi + y \cos \phi,$$

where $\phi = \phi(z)$ is the angle that the profile has been rotated. Then switch to cylindrical coordinates using $x = r \cos \theta$ and $y = r \sin \theta$ to achieve

$$\rho = \rho_0 + rB \sin[\theta - \phi(z)]. \quad (2)$$

Assuming incompressible flow, the density field is governed by

$$\rho_t + u\rho_r + \frac{v}{r}\rho_\theta + w\rho_z = 0, \quad (3)$$

where u , v , and w are the radial, azimuthal, and axial components of velocity, respectively. Note that the axial coordinate z is horizontal. Insert (2) into (3) and assume steady flow. If the vortex is circular, meaning the radial component of velocity is zero ($u = 0$), then

$$\phi_z = \frac{v}{rw}.$$

Choose the rate of rotation of the axis to be constant so that ϕ varies linearly with z , resulting in

$$\frac{v}{rw} = \frac{2\pi}{L}, \quad (4)$$

where L is the axial length for one oscillation of the density field (the pitch). The factor 2π is added for convenience. The final density field is

$$\rho = \rho_0 + rB \sin\left(\theta - \frac{2\pi z}{L}\right). \quad (5)$$

Furthermore, for this density field to exist,

$$\frac{v}{rw} = \text{const.}$$

B. Base-state velocity field

A base-state velocity field that approximately matches the density field in (5) is now found assuming weak stratification and neglecting viscosity. First rescale all variables using

$$z \rightarrow \frac{L}{2\pi}z, \quad r \rightarrow Rr, \quad t \rightarrow \frac{R}{V}t, \quad \begin{pmatrix} u \\ v \\ w \end{pmatrix} \rightarrow V \begin{pmatrix} u \\ v \\ w \end{pmatrix}, \quad p \rightarrow \rho_0 V^2 p, \quad \rho \rightarrow \rho_0 \rho,$$

where p is the pressure. The dimensionless governing equations are

$$\rho \left[u_t + uu_r + \frac{v}{r}u_\theta + wku_z - \frac{v^2}{r} \right] = -p_r - \frac{1}{\text{Fr}^2} \rho \sin \theta, \quad (6)$$

$$\rho \left[v_t + uv_r + \frac{v}{r}v_\theta + wkv_z + \frac{uv}{r} \right] = -\frac{1}{r}p_\theta - \frac{1}{\text{Fr}^2} \rho \cos \theta, \quad (7)$$

$$\rho \left[w_t + uw_r + \frac{v}{r}w_\theta + wkw_z \right] = -kp_z, \quad (8)$$

$$u_r + \frac{u}{r} + \frac{1}{r}v_\theta + kw_z = 0, \quad (9)$$

$$\rho_t + u\rho_r + \frac{v}{r}\rho_\theta + wk\rho_z = 0, \quad (10)$$

where

$$\text{Fr}^2 = \frac{V^2}{Rg} \quad (11)$$

and

$$k = \frac{2\pi R}{L}. \quad (12)$$

The density field (5) becomes

$$\rho = 1 + \beta r \sin(\theta - z), \quad (13)$$

where

$$\beta = \frac{BR}{\rho_0} \quad (14)$$

is assumed to be a small parameter. Here β is similar to the inverse of the (dimensionless) density scale height, often defined for a stratified fluid that has a stable background density profile.

The assumption that β is small implies that the density difference across the vortex is small. However, small β does not mean that Fr is small. First, the definition of $\tilde{\text{Fr}}$ in (1) uses length and velocity scales involving two counterrotating vortices, which does not apply here. Using the length and velocity scales for a single vortex and replacing the buoyancy frequency N with $\sqrt{gB/\rho_0}$ gives an equivalent definition

$$\tilde{\text{Fr}} = \frac{V}{\sqrt{g\beta R}}. \quad (15)$$

The two Froude numbers are related by

$$\tilde{\text{Fr}} = \sqrt{\beta} \text{Fr},$$

showing that the numerical values of the two parameters do not match. However, the value of $\tilde{\text{Fr}}$ using (15) may be large, even with small β .

Expand the velocity, pressure, and density fields in a power series in β :

$$\begin{pmatrix} u \\ v \\ w \\ p \\ \rho \end{pmatrix} = \begin{pmatrix} u_0 \\ v_0 \\ w_0 \\ p_0 \\ 1 \end{pmatrix} + \beta \begin{pmatrix} u_1 \\ v_1 \\ w_1 \\ p_1 \\ \rho_1 \end{pmatrix} + \beta^2 \begin{pmatrix} u_2 \\ v_2 \\ w_2 \\ p_2 \\ \rho_2 \end{pmatrix} + \dots$$

The zeroth-order equations are identical to the inviscid constant-density equations, which allow a solution with $u_0 = 0$, $v_0 = v_0(r)$, and $w_0 = w_0(r)$. Choose the leading-order (zeroth-order) velocity field to have constant axial vorticity,

$$v_0 = r, \quad w_0 = \frac{1}{k},$$

which gives

$$\frac{v_0}{rw_0} = k,$$

as required by (3). This choice allows the velocity components at first order to be found analytically.

Using the above zeroth-order velocity field, the first-order equations become

$$u_{1\theta} + u_{1z} - 2v_1 = -p_{1r} + r\rho_1 - \frac{1}{\text{Fr}^2}\rho_1 \sin \theta, \quad (16)$$

$$2u_1 + v_{1\theta} + v_{1z} = -\frac{1}{r}p_{1\theta} - \frac{1}{\text{Fr}^2}\rho_1 \cos \theta, \quad (17)$$

$$w_{1\theta} + w_{1z} = -kp_{1z}, \quad (18)$$

$$u_{1r} + \frac{u_1}{r} + \frac{1}{r}v_{1\theta} + kw_{1z} = 0, \quad (19)$$

$$\rho_{1\theta} + \rho_{1z} = 0. \quad (20)$$

The solution for ρ_1 that matches (13) is

$$\rho_1 = r \sin(\theta - z). \quad (21)$$

The other terms in (16)–(19) then experience terms containing ρ_1 as inhomogeneous effects, and each term may be treated individually. One of the terms in (16) that contains ρ_1 becomes

$$r\rho_1 = r^2 \sin(\theta - z). \quad (22)$$

The other two forcing terms that appear in (16) and (17) may be expanded using (21) to get

$$\frac{1}{\text{Fr}^2} \rho_1 \sin \theta = \frac{1}{2 \text{Fr}^2} r [-\cos(2\theta - z) + \cos z], \quad (23)$$

$$\frac{1}{\text{Fr}^2} \rho_1 \cos \theta = \frac{1}{2 \text{Fr}^2} r [\sin(2\theta - z) - \sin z]. \quad (24)$$

Thus, among the three forcing terms (22)–(24) there are $m = 0, 1,$ and 2 azimuthal harmonics.

1. Zeroth azimuthal harmonic

The terms in (23) and (24) that have no azimuthal dependence force an axisymmetric solution

$$\begin{pmatrix} u_1 \\ v_1 \\ w_1 \\ p_1 \end{pmatrix} = \frac{1}{2 \text{Fr}^2} \begin{pmatrix} r \sin z \\ r \cos z \\ \frac{1}{k} 2r \cos z \\ \frac{1}{k^2} 2r \cos z \end{pmatrix}. \quad (25)$$

Since u_1 is nonzero, an additional homogeneous part must be added to meet the boundary condition at $r = 1$. The final solution is

$$\begin{pmatrix} u_1 \\ v_1 \\ w_1 \\ p_1 \end{pmatrix} = \begin{pmatrix} f(r) \sin z \\ g(r) \cos z \\ h(r) \cos z \\ -\frac{1}{k} h(r) \cos z \end{pmatrix}, \quad (26)$$

where

$$f = \frac{1}{2 \text{Fr}^2} \left[r - \frac{J_1(\sqrt{3}kr)}{J_1(\sqrt{3}k)} \right], \quad (27)$$

$$h = \frac{1}{2 \text{Fr}^2} \left[r - 2 \frac{J_1(\sqrt{3}kr)}{J_1(\sqrt{3}k)} \right], \quad (28)$$

$$g = \frac{1}{2k \text{Fr}^2} \left[2 - \frac{\frac{d}{dr} [r J_1(\sqrt{3}kr)]}{r J_1(\sqrt{3}k)} \right]. \quad (29)$$

Here and later, J_m is the Bessel function of order m . This solution is unbounded at an infinite sequence of resonant values of k , given by

$$J_1(\sqrt{3}k) = 0. \quad (30)$$

The first ten k values are listed in the first column of Table I.

2. First azimuthal harmonic

The term $r\rho_1$ in (16) results in the forced contribution

$$v_1 = -\frac{1}{2} r^2 \sin(\theta - z), \quad (31)$$

$$w_1 = -\frac{1}{2k} r \sin(\theta - z), \quad (32)$$

with $u_1 = p_1 = 0$. Since u_1 is zero everywhere with this part, the boundary condition is satisfied and no additional homogeneous solution is required.

TABLE I. Values of k where the base flow velocity solution is unbounded.

$m_c = 0$	$m_c = 2$
2.2122	2.4352
4.0505	4.1975
5.8737	5.9808
7.6924	7.7762
9.5093	9.5779
11.3252	11.3831
13.1405	13.1907
14.9555	14.9997
16.7702	16.8097
18.5827	18.6204

3. Second azimuthal harmonic

The forced solution for the second azimuthal harmonic terms given in (23) and (24) is

$$u_1 = -\frac{1}{2 \text{Fr}^2} r \sin(2\theta - z),$$

$$v_1 = -\frac{1}{2 \text{Fr}^2} r \cos(2\theta - z),$$

with $w_1 = p_1 = 0$. A homogeneous solution is also required to meet the boundary condition at $r = 1$, finally resulting in

$$\begin{pmatrix} u_1 \\ v_1 \\ w_1 \\ p_1 \end{pmatrix} = \begin{pmatrix} f(r) \sin(2\theta - z) \\ g(r) \cos(2\theta - z) \\ h(r) \cos(2\theta - z) \\ -\frac{1}{k} h(r) \cos(2\theta - z) \end{pmatrix}, \quad (33)$$

where

$$f = \frac{1}{2 \text{Fr}^2} \left[-r + \frac{1}{r^4} \frac{d}{dr} [r^4 J_2(\sqrt{3}kr)] \right], \quad (34)$$

$$g = \frac{1}{2 \text{Fr}^2} \left[-r + \frac{2}{r} \frac{d}{dr} [r J_2(\sqrt{3}kr)] \right], \quad (35)$$

$$h = \frac{k}{2 \text{Fr}^2} \left[3 \frac{J_2(\sqrt{3}kr)}{\frac{d}{dr} [r^4 J_2(\sqrt{3}kr)]|_{r=1}} \right]. \quad (36)$$

This solution is also unbounded at an infinite sequence of resonant values of k , defined by

$$\frac{d}{dr} [r^4 J_2(\sqrt{3}kr)]|_{r=1} = \sqrt{3}k J_2'(\sqrt{3}k) + 4J_2(\sqrt{3}k) = 0, \quad (37)$$

where the prime acting on a Bessel function means derivative with respect to the argument. This expression may be solved numerically to determine these values, and the first ten values are listed in the second column of Table I.

C. Character of the base flow

The total base flow solution is the sum of the three azimuthal harmonics. Higher-order contributions may be obtained, but are not required to determine the stability of the flow. It will be shown

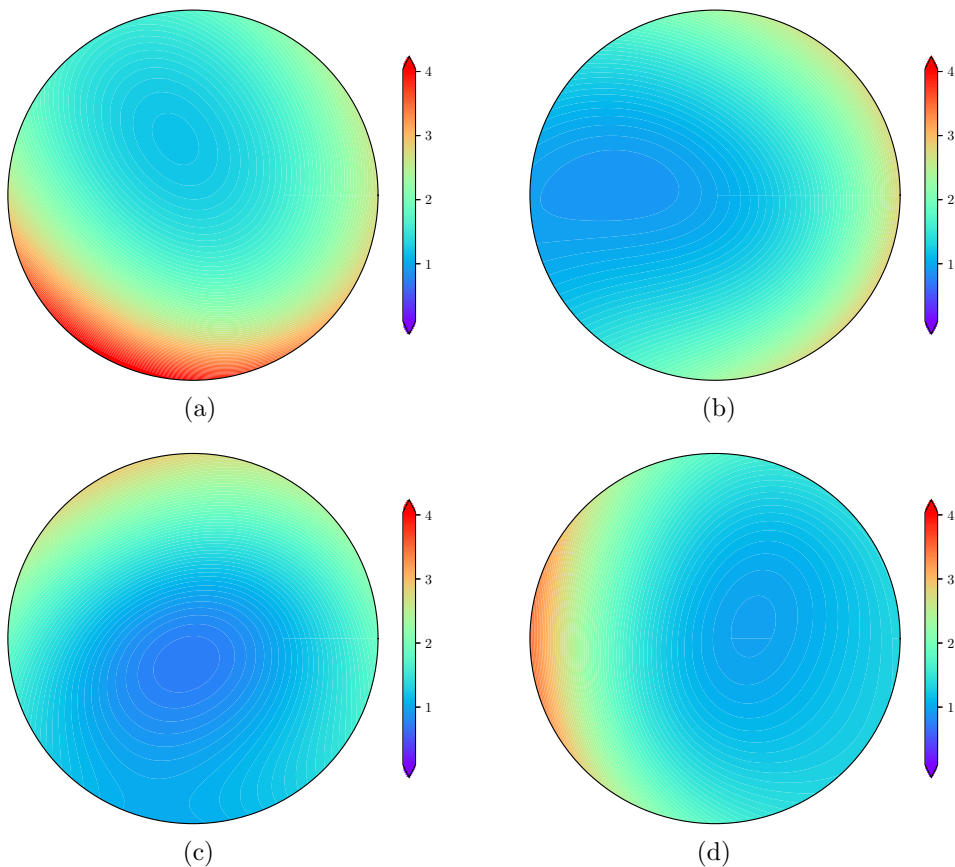


FIG. 2. Contours of kinetic energy of the base flow at four axial positions (a) $z = 0$, (b) $z = \frac{\pi}{2}$, (c) $z = \pi$, and (d) $z = \frac{3\pi}{2}$, with $\beta = 0.5$ and $k = Fr = 1$.

below that any of the three components may be unstable. The component of the flow given by (26) (the zeroth azimuthal harmonic) and (33) (the second azimuthal harmonic) represents the direct effect of the gravitational body force to distort the stratified vortex. The zeroth azimuthal harmonic is an axisymmetric flow with swirl. The flow twists and pulses axisymmetrically along the vortex axis and will be called the twirling component.

The forced part of the second azimuthal harmonic is a rolling planar flow and will be called the rolling component (when the homogeneous part is added the flow is no longer planar). This component is an elliptical distortion, similar to that of Crow [9], Moore and Saffman [10], and subsequent authors. The elliptical distortion is different here since it varies in the axial direction and has nonzero axial vorticity.

The component given by (31) and (32) (the first azimuthal harmonic) is not directly caused by gravity and could exist without gravity, as long as a stratified vortex is overturning as described above. This component exists due to the centrifugal acceleration of a spinning stratified fluid. Overall, this $m_c = 1$ flow is a helical pattern strongest near the outer boundary. Furthermore, the azimuthal dependence causes the flow to be maximum at one azimuth and minimum on the opposite side of the vortex. It can be visualized as a pair of helical streaming flows, one flow contributing to the base flow and one opposing, and will be called the streaming component.

One example flow pattern ($\beta = 0.5$ and $k = Fr = 1$) for this base state is shown in Fig. 2 using contours of kinetic energy at four axial positions. These images show that the core of vortex is not

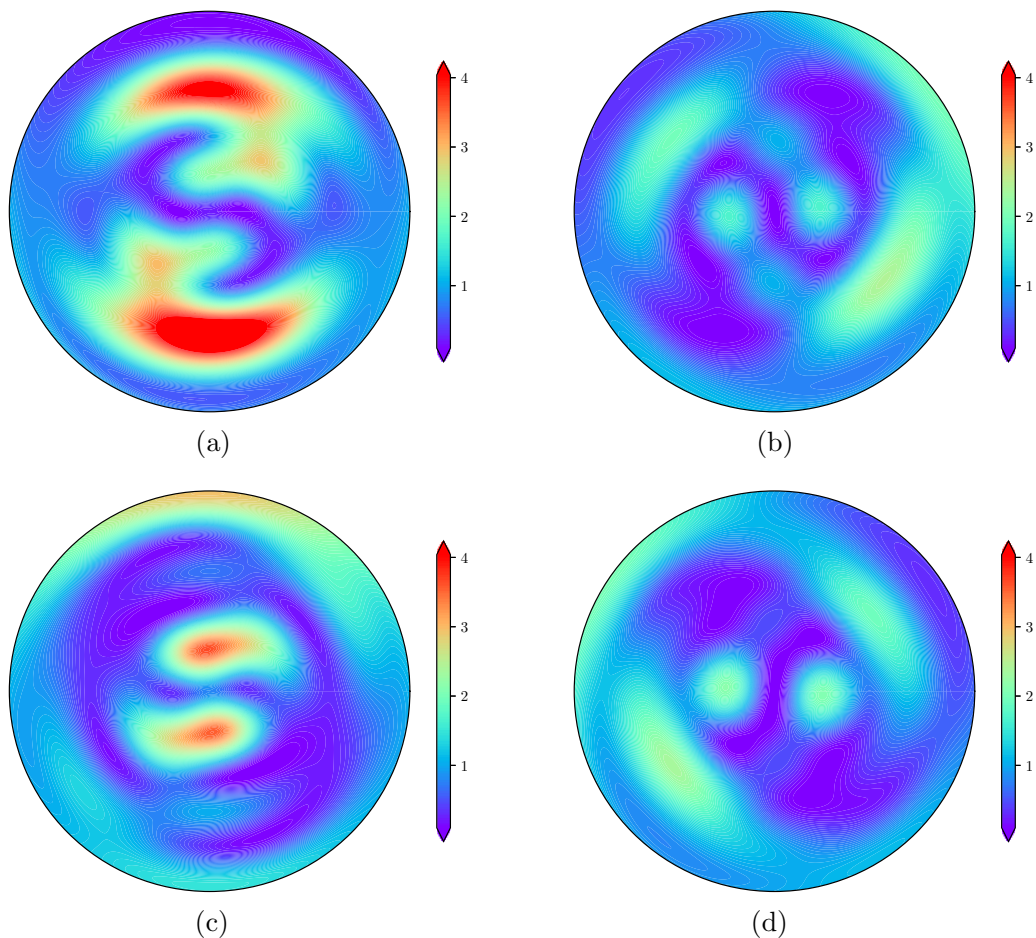


FIG. 3. Contours of kinetic energy of the base flow at four axial positions (a) $z = 0$, (b) $z = \frac{\pi}{2}$, (c) $z = \pi$, and (d) $z = \frac{3\pi}{2}$, with $\beta = 0.5$, $k = 5$, and $\text{Fr} = 1$.

centered at the origin as it cycles around the origin with increasing z . It is also apparent that the core is not circular but is flattened, and this effect also rotates with increasing z . A second example flow pattern with larger k ($\beta = 0.5$, $\text{Fr} = 1$, and $k = 5$) is shown in Fig. 3. As k increases, the pitch of the overturning density field is becoming shorter. This shorter axial length also has more oscillations in the radial direction, as can be seen in Fig. 3.

III. STABILITY

Now add a disturbance to this base flow,

$$u_i = \bar{u}_i(r, \theta, z) + u'_i,$$

and similar expressions for ρ and p , where the overbar indicates a base flow quantity, taken to be the steady distorted vortex solution discussed previously. Insert these expressions into the governing equations (6)–(9), subtract the base flow terms, and neglect products of disturbance quantities. The

base flow solution may be written as

$$\begin{pmatrix} \bar{u} \\ \bar{v} \\ \bar{w} \\ \bar{p} \\ \bar{\rho} \end{pmatrix} = \begin{pmatrix} u_0 \\ v_0 \\ w_0 \\ p_0 \\ 1 \end{pmatrix} + \beta \begin{pmatrix} u_1 \\ v_1 \\ w_1 \\ p_1 \\ \rho_1 \end{pmatrix} + O(\beta^2), \quad (38)$$

where the $O(1)$ and $O(\beta)$ quantities are given in the preceding section. The disturbance is presumed to be a normal mode

$$\begin{pmatrix} u' \\ v' \\ w' \\ p' \\ \rho' \end{pmatrix} \rightarrow \epsilon e^{i(\sigma t + m\theta + jz)} \begin{pmatrix} u(r) \\ v(r) \\ w(r) \\ p(r) \\ \rho(r) \end{pmatrix}, \quad (39)$$

where ϵ is the disturbance amplitude, j is the axial wave number, and σ is the complex frequency, expanded using

$$\sigma = \sigma_0 + \beta\sigma_1 + O(\beta^2).$$

Equation (10) becomes

$$i\hat{\sigma}\rho = O(\beta), \quad (40)$$

where

$$\hat{\sigma} = \sigma_0 + m + j. \quad (41)$$

Thus the disturbance density is higher order in β compared to the disturbance velocity components and disturbance pressure. This in turn causes the buoyancy terms in the momentum equations that contain ρ' to also be $O(\beta)$. With this in mind, the equations reduce to

$$i\hat{\sigma}u - 2v = -p_r - \beta(i\sigma_1u + Q_1), \quad (42)$$

$$i\hat{\sigma}v + 2u = -\frac{1}{r}imp - \beta(i\sigma_1v + Q_2), \quad (43)$$

$$i\hat{\sigma}w = -i\hat{k}p - \beta(i\sigma_1w + Q_3), \quad (44)$$

$$u_r + \frac{1}{r}u + im\frac{1}{r}v + i\hat{k}w = 0, \quad (45)$$

where

$$\hat{k} = kj \quad (46)$$

and the interaction terms give

$$Q_1 = \left\langle u_{1r}u' + u_1u'_r + \frac{1}{r}v_1u'_\theta + kw_1u'_z + \left(\frac{1}{r}u_{1\theta} - \frac{2}{r}v_1\right)v' + ku_{1z}w' \right\rangle, \quad (47)$$

$$Q_2 = \left\langle \frac{1}{r}(v_{1\theta} + u_1)v' + u_1v'_r + \frac{1}{r}v_1v'_\theta + kw_1v'_z + \left(v_{1r} + \frac{1}{r}v_1\right)u' + kv_{1z}w' \right\rangle, \quad (48)$$

$$Q_3 = \left\langle kw_{1z}w' + u_1w'_r + \frac{1}{r}v_1w'_\theta + kw_1w'_z + w_{1r}u' + \frac{1}{r}w_{1\theta}v' \right\rangle. \quad (49)$$

The angular brackets refer to the process that extracts the part of the $O(\beta)$ interaction terms that have azimuthal and axial wave numbers matching the primary harmonic, as discussed in the next section. Terms containing ρ_1 do not appear at this order. They combine to cancel exactly since the coefficients of ρ_1 are the same as the linear terms, which the linear solution satisfies exactly.

Eliminate u , v , p , and ρ from the linear terms in (40)–(42) to obtain

$$r^2 w_{rr} + r w_r - m^2 w + \frac{4 - \hat{\sigma}^2}{\hat{\sigma}^2} \hat{k}^2 r^2 w = \beta \frac{1}{\hat{\sigma}^2} \left[r \frac{\partial}{\partial r} [r(i\sigma_1 A_1 + A_2)] - (i\sigma_1 B_1 + B_2) \right], \quad (50)$$

where

$$\begin{aligned} A_1 &= i\hat{\sigma} w_r - i2\hat{k}v + \hat{k}\hat{\sigma}u, \\ B_1 &= i\hat{\sigma}m^2 w - i\hat{k}\hat{\sigma}mrv + 2\hat{k}mru, \\ A_2 &= i\hat{\sigma}Q_{3r} - i2\hat{k}Q_2 + \hat{k}\hat{\sigma}Q_1, \\ B_2 &= i\hat{\sigma}m^2 Q_3 - i\hat{k}\hat{\sigma}mrQ_2 + 2\hat{k}mrQ_1. \end{aligned}$$

Disturbance solution

The solution to (50) at leading order is

$$w = J_m(\gamma r), \quad (51)$$

where

$$\gamma^2 = \frac{4 - \hat{\sigma}^2}{\hat{\sigma}^2} \hat{k}^2, \quad (52)$$

and γ will be shown to be real. Note that γ may be negative, in which case

$$w = (-1)^m J_m(|\gamma|r).$$

The other velocity components are related to w by

$$\begin{aligned} u &= i \frac{1}{\gamma^2} \frac{\hat{k}}{\hat{\sigma}} \left[\hat{\sigma} w_r + 2 \frac{m}{r} w \right], \\ v &= - \frac{1}{\gamma^2} \frac{\hat{k}}{\hat{\sigma}} \left[2w_r + \hat{\sigma} \frac{m}{r} w \right]. \end{aligned}$$

This solution is identical to the linear modes of a spinning cylinder of fluid (see Refs. [26,27]). Values of γ are obtained by imposing $u(1) = 0$, giving

$$\gamma \hat{\sigma} J'_m(\gamma) + 2m J_m(\gamma) = 0. \quad (53)$$

Hence (52) and (53) are two algebraic equations for γ and $\hat{\sigma}$. Greenspan [26] proved that $\hat{\sigma}$ is always real and $|\hat{\sigma}| < 2$. The wave numbers k and j must be real to retain axial periodicity, making \hat{k} also real. This fact along with (52) means that γ is also real. Since $\hat{\sigma}$, m , and j are all real for any disturbance, then (41) means that the frequency σ_0 of each disturbance is real. Thus the base flow at leading order, which does not include any distortion, is stable, since all disturbances are purely oscillatory in time.

Instability arises at the next order, $O(\epsilon\beta)$, when the product of the $O(\beta)$ base flow quantities and the $O(\epsilon)$ disturbance quantities produces a waveform that matches the linear disturbance waveform. Such terms exist when there are two disturbances that satisfy the three-wave resonance conditions:

$$m_a = m_b + m_c, \quad (54)$$

$$j_a = j_b - 1, \quad (55)$$

$$\sigma_a = \sigma_b, \quad (56)$$

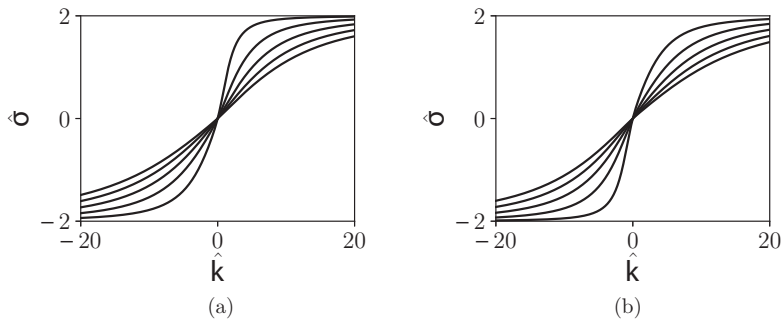


FIG. 4. First five profiles of $\hat{\sigma}$ for two azimuthal wave numbers (a) $m = 1$ and (b) $m = -1$.

where m_a , j_a , and σ_a are the wave numbers and frequency of one disturbance, while m_b , j_b , and σ_b are for the other. The base flow is the third member of the wave triad, with wave numbers $m_c = 0, 1$, or 2 , $j_c = -1$, and a frequency of zero. Phillips [37] introduced the idea of three-wave resonances for studying three interacting free-surface waves. Moore and Saffman [13] used the three-wave resonance with the vortex base flow modeling one of the waves, as here. A primary difference between here and Ref. [13] is that the base flow has an axial wave number k , while in the work of Moore and Saffman the base flow did not have an axial variation, and (55) was replaced with $j_a = j_b$.

The disturbance pairs must obey the resonance conditions (54)–(56), while each member of the pair must individually satisfy the dispersion relation (52) and the boundary condition (53). Thus (52)–(56), along with the definitions in (41) and (46), uniquely determine the disturbance pairs. To find disturbances that satisfy all the conditions, choose azimuthal wave numbers for two disturbances m_a and m_b that combine with an azimuthal component of the base flow m_c to satisfy (54). All base flow azimuthal components $m_c = 0, 1, 2$ result in a multitude of disturbance pairs.

The relationship between $\hat{\sigma}$ and \hat{k} may be determined first for each value of m , without reference to the resonance conditions. Consider, for example, $m_a = 1$ and $m_b = -1$, which successfully combine with the $m_c = 2$ of the base flow to satisfy (54). Profiles of $\hat{\sigma}(\hat{k})$ for $m = \pm 1$ are shown in Figs. 4(a) and 4(b), respectively. There is an infinite set of modes for each m (discussed by Greenspan [26]). Only the first five are shown in Figs. 4(a) and 4(b). More modes would have smaller values of $\hat{\sigma}$ and increasingly larger values of γ , making the behavior of each additional mode increasingly oscillatory with the radial coordinate. The profiles are not antisymmetric and must be determined uniquely for negative \hat{k} as well as positive. Each profile along with the definitions (41) and (46) may be used to construct a dispersion profile $\sigma_0(j)$ for each value of the base-state wave number k .

Dispersion profiles $\sigma_0(j)$ for two example values of k are shown in Fig. 5, choosing the first profile of $\hat{\sigma}(\hat{k})$ in Figs. 4(a) and 4(b). Each panel in Fig. 5 has two solid lines and two dashed lines. The solid lines are the dispersion profiles for $m = +1$, while the dashed lines are for $m = -1$. There are two lines for each because $\hat{\sigma}$ may be positive or negative at a fixed value of $\hat{\sigma}(\hat{k})$. One solid line is a dispersion profile as in Fig. 4. This profile is “positive” in that positive \hat{k} correspond to positive $\hat{\sigma}$. The other solid line is formed by taking the negative of this first set of $\hat{\sigma}$ values. This second solid line is “negative” in that positive \hat{k} correspond to negative $\hat{\sigma}$. Each profile is then used along with (41) and (46) to extract the profiles $\sigma_0(j)$, one negative and one positive.

The process is repeated for the dashed lines, which are then shifted along the abscissa by unity to account for the resonance condition in (55). The intersection of a solid line with a dashed line gives a valid solution to the resonance conditions, since the frequency’s σ_0 match at the intersections, satisfying (56), while each figure is constructed to satisfy the other two resonance conditions (54) and (55).

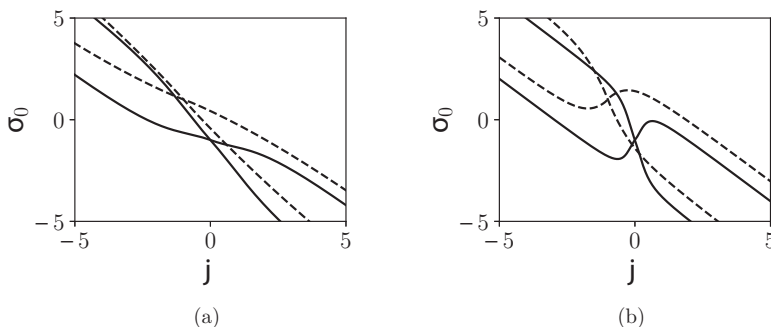


FIG. 5. Dispersion profiles for $m_a = 1$, $m_b = -1$, and $m_c = 2$ for two example values of k : (a) $k = 1$ and (b) $k = 5$.

The example in Fig. 5(b) has $k = 5$ and shows four intersections. Thus, for this case there are four sets of disturbances, each set consisting of a pair of disturbance waves. No parameter values have been found with more than four sets. The four sets are arbitrarily labeled modes 0, 1, 2, and 3. Modes 0 and 1 are intersections of dispersion profiles with the same sign: positive-positive or negative-negative. Mode 2 is a negative-positive intersection and mode 3 is a positive-negative intersection. A more physically meaningful characterization of the four modes has not emerged. The search for allowable modes is performed with one of each dispersion profile, finding one mode at a time, suggesting this characterization. Precise values of σ_0 for the intersections of these profiles are found numerically using the bisection method.

The numerical results show that for all values of k considered with $m_c = 1$, each combination of allowable profiles $\hat{\sigma}(\hat{k})$ results in four independent modes that satisfy the three-wave conditions. The frequency σ_0 of these allowable disturbance modes is shown in Fig. 6 for four values of m_a and m_b . Note that mode 0 is shown with a black line, 1 is blue, 2 is red, and 3 is green, in Fig. 6 and beyond. Mode numbers are also shown near each line. The results shown in Fig. 6 use the first dispersion profile for each m , giving the smallest values of γ . Choosing other profiles results in a different set of modes with larger values of γ .

With $m_c = 0$ and 2, larger values of k also result in four modes, as in Fig. 5(b). However, smaller values of k with $m_c = 0$, 2 only have two modes, as in Fig. 5(a). The negative solid profile no longer intersects the negative dashed profile in Fig. 5(a), unlike Fig. 5(b). Thus there is no mode 0 or 1 for this value of k with $m_a = 1$, $m_b = -1$, and $m_c = 2$.

Figures 7 and 8 show the frequency σ_0 of allowable modes with $m_c = 0$ and 2, respectively, for four cases each. As before, all modes in Figs. 7 and 8 use the first $\hat{\sigma}(\hat{k})$ profiles. It can be clearly seen that modes 0 and 1 merge and do not exist for smaller values of k in both figures.

There are values of k with $m_c = 0, 2$ where one of the disturbances is resonant. At such a resonant value, the axial wave number j of the resonant disturbance becomes zero. With $j = 0$, the axial disturbance velocity is also zero, $w = 0$, and the solution for the disturbance velocity in (51) is no longer valid. The equation governing the other velocity components u and v at these special points is of Cauchy-Euler type. With $m \neq 0$, the resulting solution is unbounded at the origin, while with $m = 0$ the solution cannot meet the boundary condition $u(1) = 0$. Thus the formulation treated here does not provide a disturbance solution at these discrete values of k . Any of the four modes may have resonant values and there may be more than one resonant value for any mode.

If $k = 0$, there is no axial variation and the base flow reduces to a purely two-dimensional motion. Furthermore, the $m_c = 2$ component of the base flow becomes zero with $k = 0$. Thus the present configuration with $k = 0$ does not match previous configurations. Previous authors considered uniform axial distortion, caused by the presence of a second vortex, which is neglected here. This previous work, such as those of Moore and Saffman [13] and Lacaze *et al.* [18], also included potential flow for $r > 1$, different than here, thus the two cases do not match, even with $k = 0$.

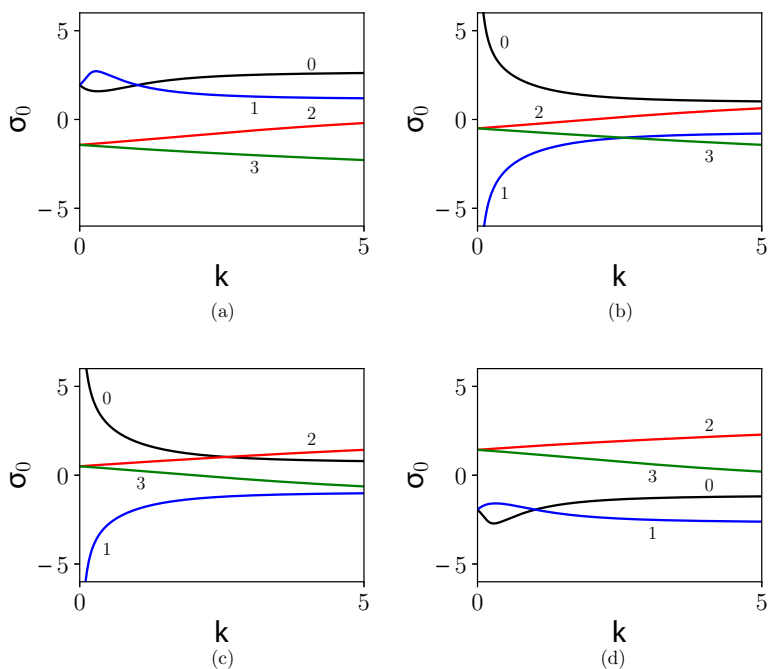


FIG. 6. Frequency of disturbance waves with $m_c = 1$: (a) $m_a = 2$ and $m_b = 1$, (b) $m_a = 1$ and $m_b = 0$, (c) $m_a = 0$ and $m_b = -1$, and (d) $m_a = -1$ and $m_b = -2$.

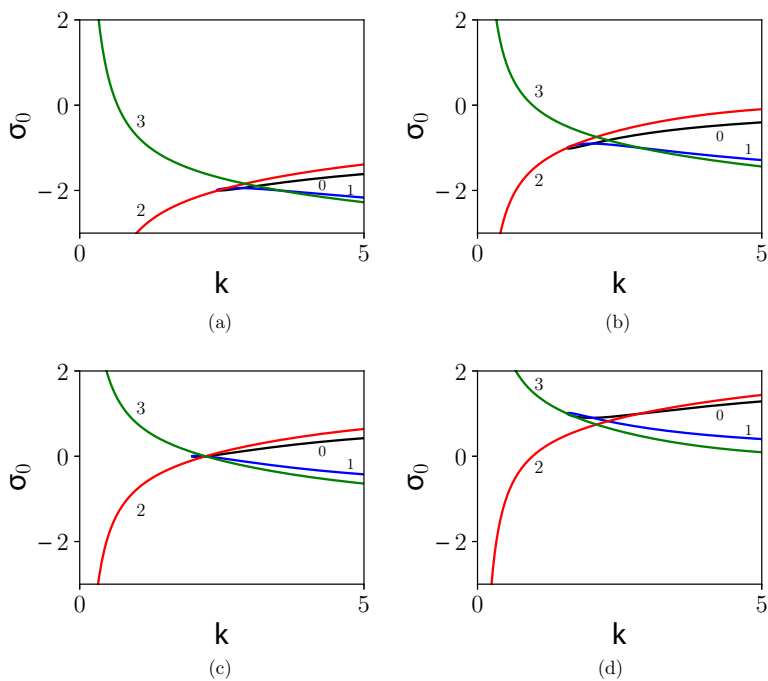


FIG. 7. Frequency of disturbance waves with $m_c = 0$: (a) $m_a = m_b = 2$, (b) $m_a = m_b = 1$, (c) $m_a = m_b = 0$, and (d) $m_a = m_b = -1$.

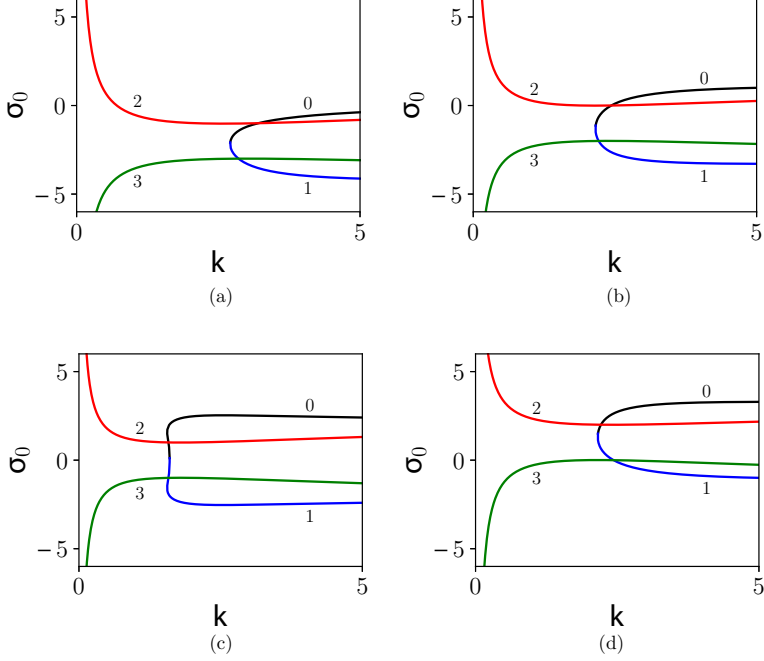


FIG. 8. Frequency of disturbance waves with $m_c = 2$: (a) $m_a = 3$ and $m_b = 1$, (b) $m_a = 2$ and $m_b = 0$, (c) $m_a = 1$ and $m_b = -1$, and (d) $m_a = 0$ and $m_b = -2$.

IV. RESULTS OF THE STABILITY ANALYSIS

The sum of the two disturbances is substituted into (50) and the resulting expression is multiplied by the waveform for each disturbance in successive steps and integrated over the spatial domain. The azimuthal and axial parts of the integral represent the angular brackets in (47)–(49), may be performed exactly, and act to collect all contributions with the same wave numbers. The radial part of the integrations is more complex and the final algebraic equations are determined by multiplication by $rJ_m(\gamma r)$ using m and γ for each disturbance in successive steps and then integration. The result is two algebraic equations

$$\begin{bmatrix} \sigma_1 D_a & E_a \\ E_b & \sigma_1 D_b \end{bmatrix} \begin{pmatrix} \epsilon_a \\ \epsilon_b \end{pmatrix} = 0, \quad (57)$$

where ϵ_a and ϵ_b are the amplitudes of the two disturbances. Thus,

$$\sigma_1^2 = \frac{E_a E_b}{D_a D_b}, \quad (58)$$

where

$$D_a = \int_0^1 \left(r \frac{\partial}{\partial r} (r A_1) - B_1 \right) r J_{m_a} dr,$$

$$D_b = \int_0^1 \left(r \frac{\partial}{\partial r} (r A_1) - B_1 \right) r J_{m_b} dr,$$

$$E_a = \int_0^1 \left(r \frac{\partial}{\partial r} (rA_2) - B_2 \right) r J_{m_a} dr,$$

$$E_b = \int_0^1 \left(r \frac{\partial}{\partial r} (rA_2) - B_2 \right) r J_{m_b} dr.$$

The integrals are performed numerically using the trapezoid rule.

A. Twirling instability $m_c = 0$

As discussed above, disturbance pairs will combine with the part of the base flow that has $m_c = 0, 1,$ or 2 to form three-wave combinations. Once the disturbances are determined, (58), along with corresponding expressions for Q_i (47)–(49), is used to determine the value of σ_1^2 . The flow is unstable when a disturbance has a value of σ with a positive imaginary part. Since σ_0 is purely real, only σ_1 can have a nonzero imaginary part, which occur as positive and negative pairs when the value of σ_1^2 is negative.

First consider the case of $m_c = 0$, which is an axisymmetric flow that oscillates along the vortex axis and is being called the twirling component. The following expressions for Q_i are valid for both disturbances when considering $m_c = 0$. When finding the values of Q_i for the a disturbance, use the upper sign and the wave parameters $m, j,$ and σ_0 for the b disturbance. Conversely, for the b disturbance,

$$Q_1 = \epsilon \frac{1}{2} \left[\pm i(fu)_r + i \frac{m}{r} gu + i j k h u \pm \frac{2}{r} gv + k f w \right],$$

$$Q_2 = \epsilon \frac{1}{2} \left[i \frac{m}{r} gv \pm i f \frac{1}{r} (rv)_r + i j k h v + \frac{1}{r} (rg)_r u \mp i k g w \right],$$

$$Q_3 = \epsilon \frac{1}{2} \left[i(j \mp 1) k h w \pm i f w_r + h_r u + i \frac{m}{r} g w \right].$$

With $m_c = 0$, use (27) and (28) for $f, g,$ and h .

Values of σ_1^2 for the case with $m_c = 0$ are shown in Fig. 9 for four combinations of m_a and m_b , matching the cases in Fig. 7. The flow is only stable if σ_1^2 is positive for all triads at a chosen value of k . Note that stability here does not require positive σ_1^2 for all k , as k is a fixed parameter for the base flow.

Figure 9 shows that for smaller values of k , the values of σ_1^2 are small and positive, indicating that these modes are stable. Larger values of σ_1^2 exist at larger values of k , as the value of σ_1^2 shows oscillatory behavior with increasing k . Different modes are the most unstable over different intervals of k . This is shown in Fig. 10, which provides the value of $\text{Im}(\sigma)$ for the most unstable modes with $m_c = 0$. The most unstable mode is the disturbance that has the largest value of $\text{Im}(\sigma)$ at a chosen k . For small k , there are no modes that have been found with nonzero imaginary part, thus the twirling component of the base flow is stable for small k . The twirling instability is relatively strong over the interval considered when $k \gtrsim 1.57$. Mode 0 with $m_a = m_b = 1$ is the strongest mode near $k \approx 2.2$; however, another mode dominates as k increases. There are many other modes: different $\hat{\sigma}(\hat{k})$ profiles and larger positive or negative values of m_a and m_b . Some of these modes have also been considered and found to be increasingly more stable. Thus the most unstable modes with $m_c = 0$ use the first $\hat{\sigma}(\hat{k})$ profile.

In general, disturbances may be propagating with the base rotation or against it (Saffman [27] calls this cograde or retrograde, respectively) and propagating upstream or downstream. With $m_c = 0$, the two disturbances have the same value of m and the same frequency to satisfy the resonance conditions, thus they propagate with the same azimuthal speed. For the case $m_a = m_b = 0$, the disturbances do not propagate in the azimuthal direction. For other cases with $m_c = 0$, with $k \gtrsim 1$ the azimuthal velocity for both disturbances is negative for all four modes, meaning that both

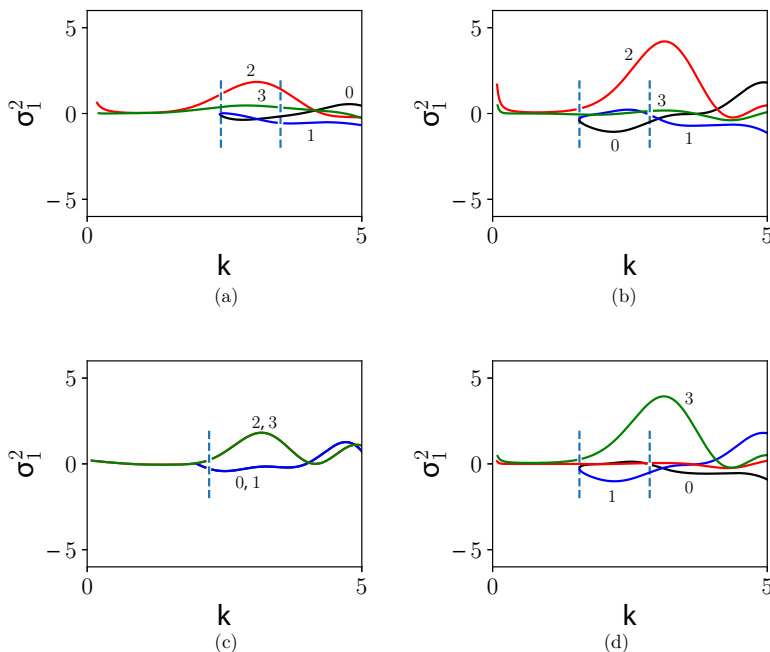


FIG. 9. Values of σ_1^2 with $m_c = 0$, $\text{Fr} = 1$: (a) $m_a = m_b = 2$, (b) $m_a = m_b = 1$, (c) $m_a = m_b = 0$, and (d) $m_a = m_b = -1$.

disturbances rotate against the base flow and are retrograde. With $k \lesssim 1$, one disturbance becomes cograde; however, the twirling component is stable for such small k .

With $k \approx 2.2$, mode 0 with $m_a = m_b = 1$ is most unstable and both disturbances are traveling upstream, one mode faster than the base flow and the other mode slower. As k increases, mode 1 with $m_a = m_b = 1$ is most unstable and both disturbances are traveling downstream.

Some of the profiles in Fig. 9 show a gap, the position of which is indicated with a dashed line segment. The position of this gap is the value of k where one of the disturbances is resonant,

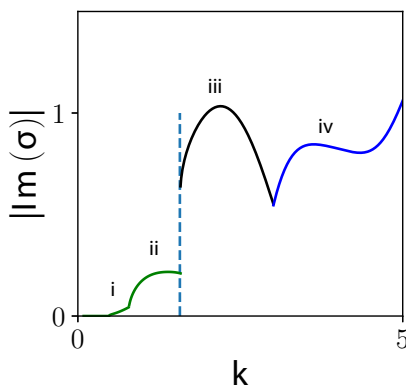


FIG. 10. Growth rates (imaginary part of σ) for the most unstable modes with $m_c = 0$ and $\text{Fr} = 1$: (i) mode 2 with $m_a = m_b = -1$ and mode 3 with $m_a = m_b = 1$, (ii) mode 3 with $m_a = m_b = 0$, (iii) mode 0 with $m_a = m_b = 1$ and mode 1 with $m_a = m_b = -1$, and (iv) mode 1 with $m_a = m_b = 1$ and mode 0 with $m_a = m_b = -1$. To obtain dimensional values, multiply by V/R .

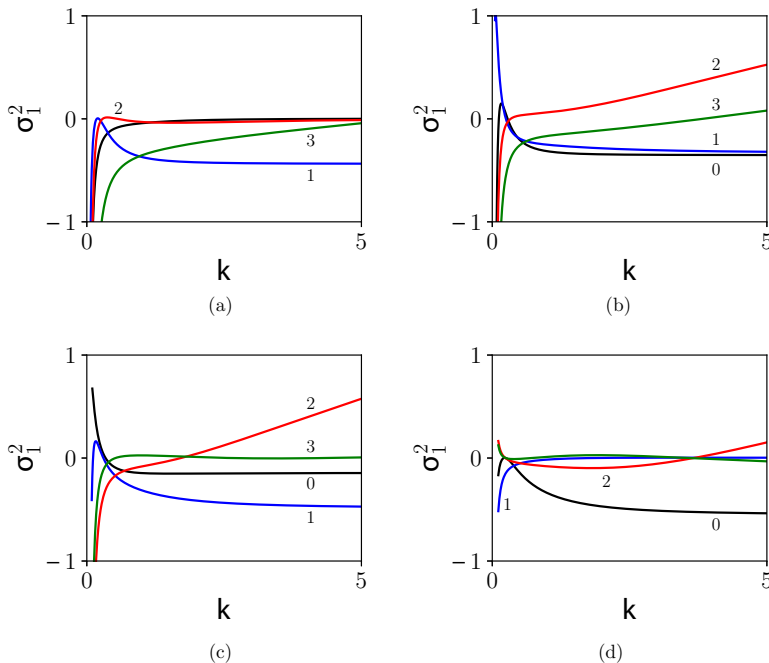


FIG. 11. Values of σ_1^2 with $m_c = 1$: (a) $m_a = 2$ and $m_b = 1$, (b) $m_a = 1$ and $m_b = 0$, (c) $m_a = 0$ and $m_b = -1$, and (d) $m_a = -1$ and $m_b = -2$.

with an axial wave number of zero, $j = 0$. As mentioned previously, the solution found here is not valid at these discrete values. Furthermore, in the immediate neighborhood of a resonant value, the associated value of γ becomes large, the behavior of the solution becomes highly oscillatory, and numerical accuracy suffers. Thus reliable results in the immediate neighborhood of a resonant disturbance are difficult to achieve with the chosen numerical approach. The rolling instability ($m_c = 2$) also has resonant cases; however, the streaming instability ($m_c = 1$) does not show resonant disturbances within the parameter values considered.

B. Streaming instability $m_c = 1$

The base flow component with $m_c = 1$ is a pair of helical streams and is called the streaming component. The process for calculating σ_1^2 with $m_c = 1$ is the same as described above, except now use

$$\begin{aligned}
 Q_1 &= \mp \epsilon \frac{1}{4} [(m + j)ru + i2rv], \\
 Q_2 &= \mp \epsilon \frac{1}{4} [(m \pm 1 + j)rv + i3ru + kr^2w], \\
 Q_3 &= \mp \epsilon \frac{1}{4} \left[(m \mp 1 + j)rw - \frac{1}{k}(iu \mp v) \right].
 \end{aligned}$$

Values of σ_1^2 for the case with $m_c = 1$ are shown in Fig. 11, again for four examples, matching the examples in Fig. 6. Figure 11 shows much different behavior than before. Now, with $m_c = 1$, the largest values of σ_1^2 occur for small k , and σ_1^2 not oscillatory with k .

The most unstable modes with $m_c = 1$ are shown in Fig. 12. For small k , the most unstable mode is mode 3 with $m_a = 2$ and $m_b = 1$ (Fig. 12, green line). Both disturbances are retrograde, with

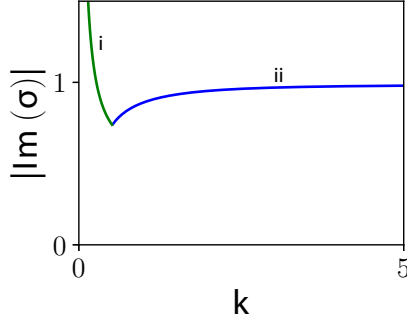


FIG. 12. Growth rates (imaginary part of σ) for the most unstable modes with $m_c = 1$: (i) mode 3 with $m_a = 2$ and $m_b = 1$ and (ii) mode 1 with $m_a = 3$ and $m_b = 2$. To obtain dimensional values, multiply by V/R .

one disturbance traveling downstream rapidly and the other traveling upstream but slower than the base flow. As k increases in value, mode 1 with $m_a = 3$ and $m_b = 2$ becomes the most unstable mode (blue line). Both disturbances are cgrade and both are traveling downstream slowly at nearly identical speeds.

As before, there are many modes other than those shown in Fig. 11, modes with different $\hat{\sigma}(\hat{k})$ profiles and larger positive or negative values of m_a and m_b . For this case ($m_c = 1$), these other modes are more stable.

C. Rolling instability $m_c = 2$

For $m_c = 2$, calculate σ_1^2 as described above, except now use

$$Q_1 = \epsilon \frac{1}{2} \left[\mp i(fu)_r + i \frac{m}{r} gu + i j k h u \pm \frac{2}{r} (f \mp g)v - k f w \right],$$

$$Q_2 = \epsilon \frac{1}{2} \left[i(m \pm 2) \frac{1}{r} g v \mp i f \frac{1}{r} (r v)_r + i j k h v + \frac{1}{r} (r g)_r u \mp i k g w \right],$$

$$Q_3 = \epsilon \frac{1}{2} \left[i(j \mp 1) k h w \mp i f w_r + i \frac{m}{r} g w + h_r u \pm i \frac{2}{r} h v \right],$$

and (34)–(36) for f , g , and h .

Profiles of σ_1^2 with $m_c = 2$ are shown in Fig. 13, again for four cases. Note the larger scale for the ordinate, compared to either Fig. 9 or 11. Figure 13 shows that the value of σ_1^2 approaches zero as $k \rightarrow 0$. This feature is present for modes 2 and 3 for all cases considered. Modes 0 and 1 do not have wave triads for small values of k , as discussed previously. For larger k , Fig. 13 shows that σ_1^2 becomes larger in absolute value in an oscillatory manner, similar to the case of $m_c = 0$.

Again, the most unstable modes are shown with values of $\text{Im}(\sigma)$, now in Fig. 14. The behavior is similar to the case of $m_c = 0$, except the growth rates are much stronger with $m_c = 2$. Thus the rolling instability is more important than the twirling instability in that both behave similarly with k , yet the rolling instability has larger growth rates. Furthermore, the rolling instability is unstable even with small k , although the streaming instability is the most dominant for small k .

Figure 14 shows that a variety of modes become dominant as k ranges over $0 < k < 5$. All of these different modes are either retrograde or do not propagate azimuthally; none are cgrade. Table II gives the sense of the azimuthal wave speed σ_0/m for each mode shown in Fig. 14. A negative sign in Table II means the disturbance is retrograde, while 0 indicates zero azimuthal wave speed. The disturbances may be propagating upstream or downstream, also indicated in Table II with the sense of σ_0/j , the axial wave speed.

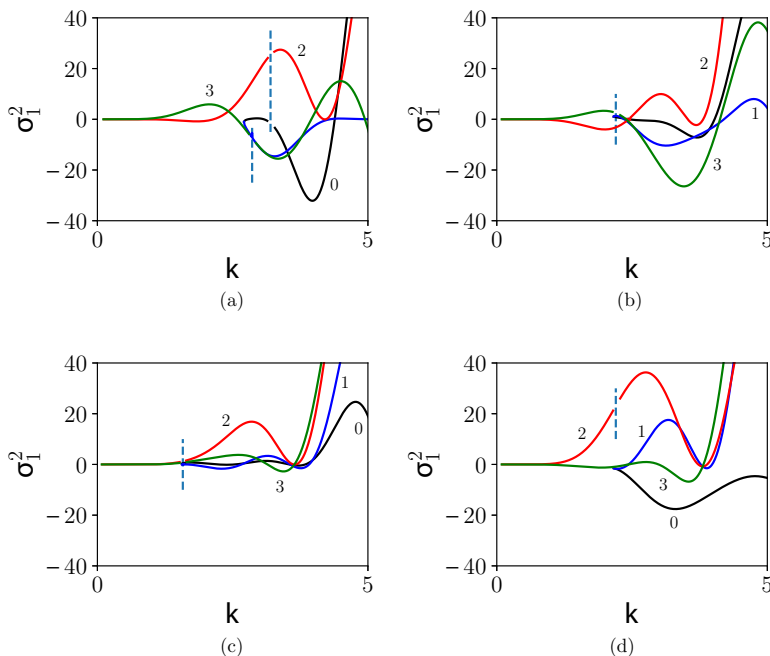


FIG. 13. Values of σ_1^2 with $m_c = 2$, $Fr = 1$: (a) $m_a = 3$ and $m_b = 1$, (b) $m_a = 2$ and $m_b = 0$, (c) $m_a = 1$ and $m_b = -1$, and (d) $m_a = -0$ and $m_b = -2$.

Cases i–iv in Fig. 14 are disturbance pairs involving the first dispersion profile $\hat{\sigma}(\hat{k})$ for each of the two disturbances. Other profiles and other values of m have resulted in weaker or stable modes, similar to the twirling and streaming instabilities. However, case v in Fig. 14 uses the second dispersion profile for the b disturbance, producing the most unstable mode for the interval shown. Using the first dispersion profile for both disturbances results in a smaller value of σ_1^2 and thus

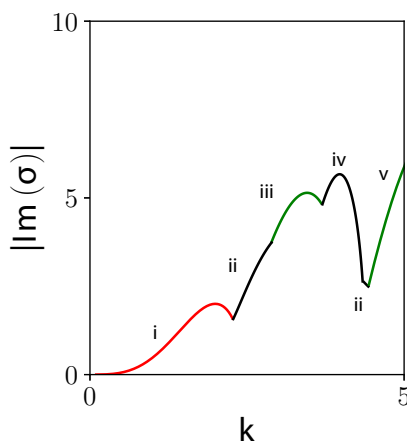


FIG. 14. Growth rates (imaginary part of σ) for the most unstable modes with $m_c = 2$ and $Fr = 1$: (i) mode 2 with $m_a = 2$ and $m_b = 0$, (ii) mode 0 with $m_a = 3$ and $m_b = 1$, (iii) mode 3 with $m_a = 2$ and $m_b = 0$, (iv) mode 0 with $m_a = 0$ and $m_b = -2$, and (v) mode 3 with $m_a = 2$ and $m_b = 0$ and using the second dispersion mode for the b disturbance. To obtain dimensional values, multiply by V/R .

TABLE II. Sense of disturbance azimuthal and axial speeds for most unstable modes with $m_c = 2$.

Mode	σ_0/m		σ_0/j	
	a	b	a	b
i	–	0	–	–
ii	–	–	+	–
iii	–	0	+	–
iv	0	–	–	–
v	–	0	+	–

a smaller growth rate for this interval. This is shown in Fig. 15, which gives the value of σ_1^2 for three cases. Case (i) uses the first dispersion profile for both disturbances, while cases (ii) and (iii) substitute the second and third profiles, respectively, for disturbance b . Clearly, case (ii) has the largest negative value of σ_1^2 for $k \gtrsim 4$. This is the only example that has been found where a disturbance pair is dominant and uses a dispersion profile other than the first one. Note that other modes dominate for $k \gtrsim 5$.

D. Further discussion

With the twirling instability ($m_c = 0$) and the rolling instability ($m_c = 2$), the strength of the base flow is proportional to the inverse of the square of the Froude number. Ultimately this means that

$$\text{Im}(\sigma) \propto \frac{1}{\text{Fr}^2}.$$

The above values for $\text{Im}(\sigma)$ with $m_c = 0, 2$ determined with $\text{Fr} = 1$ can be used to find $\text{Im}(\sigma)$ for any other Froude number merely with division by Fr^2 . Thus the growth rates decrease dramatically as Fr increases. Unstable modes given above for $\text{Fr} = 1$ are still unstable at large Fr , but growth rates are smaller. The streaming instability is independent of Fr .

The behavior with k of the streaming instability is much different from the behavior with k of the twirling and rolling instabilities. The streaming instability is strong for small k , which corresponds to a long pitch of the base flow. The twirling and rolling instabilities are strong for larger k , corresponding to a short pitch.

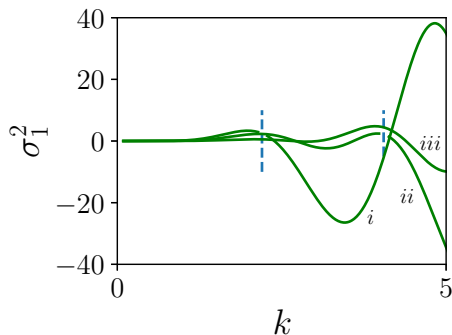


FIG. 15. Values of σ_1^2 for mode 3 with $m_c = 2$, $m_a = 2$, and $m_b = 0$. The a disturbance uses the first dispersion profile $\hat{\sigma}(\hat{k})$, while the b disturbance uses the (i) first, (ii) second, and (iii) third profiles. To obtain dimensional values, multiply by V/R .

The solution for the base flow velocity for the twirling and rolling modes becomes unbounded at a sequence of values of k , as discussed previously. This happens when the divisor in (30) or (37) becomes zero. This divisor appears in each term of both algebraic equations in (57) and thus cancels in (58). As a result, finite values of σ_1^2 are achieved at these resonant values of k . Furthermore, the maxima of σ_1^2 that appear in Figs. 10 and 14 do not generally correspond to these resonant k values.

V. CONCLUSION

Previous numerical simulations of a pair of counterrotating vortices released in a density stratified fluid approximated the flow behind a wing. These simulations were either two dimensional or had the density field initially uniform along the axis of the vortices. However, the density field behind a wing in laboratory experiments or in the field is quite different. The trailing vortex system behind a wing twists the density field such that it overturns along the axis of the vortices. Thus the base flow behind a wing has a density profile that oscillates between statically stable and unstable states. This density field is approximated here assuming a steady flow that has the density overturning periodically along the axis of a vortex. The matching base-state velocity is found approximately assuming weak stratification.

This steady base flow is shown here to be unstable. Attention is restricted to the case where the base velocity field has constant axial vorticity at leading order and the flow is contained within a rigid cylinder. With weak stratification, the disturbance modes are identical to waves in a spinning cylinder of fluid. An instability exists when the disturbances satisfy the three-wave resonance conditions, with two disturbance waves interacting with a component of the base flow to form the wave triad.

The base-state velocity field has components with azimuthal wave number $m_c = 0, 1, 2$. Disturbance pairs that satisfy the resonance conditions exist with all of these components individually. The $m_c = 1$ component is a streaming flow, featuring a pair of helical streams superimposed on the base vortex. The results show that many of the disturbance pairs that combine with the streaming component are unstable such that the flow is always unstable. This streaming instability depends strongly on k and is dominant for small k , corresponding to a large pitch of the base flow. However, the streaming instability is independent of the Froude number Fr .

The twirling ($m_c = 0$) component is an axisymmetric flow with swirl, oscillatory along the vortex axis. This twirling component is stable for small k and unstable as k becomes larger (short pitch). Growth rates for the twirling instability are smaller than those for the rolling instability ($m_c = 2$), thus the rolling instability dominates the behavior as k becomes large.

The rolling $m_c = 2$ component is similar to the elliptic instability. The $m_c = 2$ distortion here is distinct because it is caused by stratification and varies along the vortex axis, whereas the elliptic distortion in previous studies was caused by the presence of a second vortex and was axially uniform. Another difference is that the velocity field here has axial vorticity that is not constant and previous cases with a Rankine vortex did have constant axial vorticity. The results here show that many of the disturbance pairs that combine with the rolling component are also unstable. The strength of this rolling instability varies with k in a complex manner. Furthermore, the strength of the instability is inversely proportional to the square of the Froude number Fr .

More generally, the present theory demonstrates that vortices in the wake of a wing in a stratified fluid are governed not only by the Froude number, but also by the pitch of the density field, as measured by k . Previous studies recognized the importance of the Froude number, but not k .

The previous three-dimensional simulations by Nomura *et al.* [4] had an initial density field that was axially uniform, which corresponds to an infinite pitch and therefore $k = 0$. However, the present theory with $k = 0$ has zero $m_c = 2$ distortion and therefore no rolling instability. Nomura *et al.* treated a vortex pair and the presence of the second vortex generated the elliptic instability, which dominated the simulations, according to Nomura *et al.* Thus the results here do not correspond to the configuration of Nomura *et al.*

Previous two-dimensional simulations of a vortex pair correspond trivially to axial uniformity. Although the simulations include two vortices, which suggests an elliptic instability, elliptic disturbances are three dimensional and do not exist in two dimensions. Similarly, the twirling and streaming instabilities found here are three dimensional, even with $k = 0$, for which the disturbance axial wave numbers are equal, $j_a = j_b$, but not zero. Thus the complex behavior at small values of Fr in the two-dimensional simulations is not completely explained by the present results. The behavior might be due to a different mechanism, involving the slow nearly static overturning of a strongly stratified fluid.

The previous laboratory experiments of Sarpkaya [8] would not have had a density field that was axially uniform, thus each case of Sarpkaya had a nonzero value for k , although this parameter is not mentioned by Sarpkaya. Using their published data, the value of k in the experiments of Sarpkaya [8] is estimated here to be $k \approx 0.1$. This means that the density field inside the vortex would be overturned in approximately five core radii along the vortex axis. Values of k for commercial aircraft are smaller, while values for wind turbines and other relatively slow-moving applications are much larger. For the small- k value of Sarpkaya's experiments, the streaming instability $m_c = 1$ is dominant. However, the experiments also had a second vortex, which is neglected here. The second vortex could also be responsible for the results of the experiments.

Trailing vortices behind airplanes are not confined to a fixed radius, suggesting an extension of the present work to an open geometry. The overturning feature of the stratified flow that has been treated here will also exist in an open geometry and therefore the same instabilities are expected to exist. However, the analysis is significantly more complex and beyond the scope of the present work.

ACKNOWLEDGMENT

The anonymous referee is acknowledged for constructive criticism.
The author reports no conflict of interest.

-
- [1] J. F. Garten, S. Arendt, D. C. Fritts, and J. Werne, Dynamics of counter-rotating vortex pairs in stratified and sheared environments, *J. Fluid Mech.* **361**, 189 (1998).
 - [2] F. M. Hill, A numerical study of the descent of a vortex pair in a stably stratified atmosphere, *J. Fluid Mech.* **71**, 1 (1975).
 - [3] F. Holzapfel and T. Gerz, Two-dimensional wake vortex physics in the stably stratified atmosphere, *Aerosp. Sci. Technol.* **3**, 261 (1999).
 - [4] K. K. Nomura, H. Tsutsui, D. Mahoney, and J. W. Rottman, Short-wavelength instability and decay of a vortex pair in a stratified fluid, *J. Fluid Mech.* **553**, 283 (2006).
 - [5] R. E. Robins and D. P. Delisi, Numerical simulations of three-dimensional trailing vortex evolution, *AIAA J.* **35**, 1552 (1997).
 - [6] P. R. Spalart, On the motion of laminar wing wakes in a stratified fluid, *J. Fluid Mech.* **327**, 139 (1996).
 - [7] S. Shaw and J. P. McHugh, Evolution of a line vortex in stratified flow, *Phys. Rev. Fluids* **4**, 064803 (2019).
 - [8] T. Sarpkaya, Trailing vortices in homogeneous and density-stratified media, *J. Fluid Mech.* **136**, 85 (1983).
 - [9] S. C. Crow, Stability theory for a pair of trailing vortices, *AIAA J.* **8**, 2172 (1970).
 - [10] D. W. Moore and P. G. Saffman, in *Aircraft Wake Turbulence and Its Detection*, edited by J. H. Olsen, A. Goldburg, and M. Rogers (Springer, Boston, 1971), pp. 339–354.
 - [11] D. W. Moore and P. G. Saffman, The motion of a vortex filament with axial flow, *Philos. Trans. R. Soc. London* **272**, 403 (1972).
 - [12] S. E. Widnall, D. B. Bliss, and C. Y. Tsai, The instability of short waves on a vortex ring, *J. Fluid Mech.* **66**, 35 (1974).

-
- [13] D. W. Moore and P. G. Saffman, The instability of a straight vortex filament in a strain field, *Proc. R. Soc. London* **346**, 413 (1975).
- [14] C. Y. Tsai and S. E. Widnall, The stability of short waves on a straight vortex filament in a weak externally imposed strain field, *J. Fluid Mech.* **73**, 721 (1976).
- [15] R. R. Kerswell, Elliptic instability, *Annu. Rev. Fluid Mech.* **34**, 83 (2002).
- [16] M. Lessen, N. V. Deshpande, and B. Hadji-Ohanes, Stability of a potential vortex with a non-rotating and rigid-body rotating top-hat jet core, *J. Fluid Mech.* **60**, 459 (1973).
- [17] T. Loiseleux, J. M. Chomaz, and P. Huerre, The effect of swirl on jets and wakes: Linear instability of the rankine vortex with axial flow, *Phys. Fluids* **10**, 1120 (1998).
- [18] L. Lacaze, A. Birbaud, and S. Le Dizès, Elliptic instability in a rankine vortex with axial flow, *Phys. Fluids* **17**, 017101 (2005).
- [19] C. Eloy and S. Le Dizès, Three-dimensional instability of burgers and lamb-oseen vortices in a strain field, *J. Fluid Mech.* **378**, 145 (1999).
- [20] D. Sipp and L. Jacquin, Widnall instabilities in vortex pairs, *Phys. Fluids* **15**, 1861 (2003).
- [21] S. Le Dizès and F. Laporte, Theoretical predictions for the elliptical instability in a two-vortex flow, *J. Fluid Mech.* **471**, 169 (2002).
- [22] S. Ortiz, C. Donnadieu, and J. M. Chomaz, Three-dimensional instabilities and optimal perturbations of a counter-rotating vortex pair in stratified flows, *Phys. Fluids* **27**, 106603 (2015).
- [23] G. I. Taylor, Stability of a viscous liquid contained between two rotating cylinders, *Philos. Trans. R. Soc. London Ser. A* **223**, 289 (1923).
- [24] P. Billant, Zigzag instability of vortex pairs in stratified and rotating fluids. Part 1. General stability equations, *J. Fluid Mech.* **660**, 354 (2010).
- [25] P. Billant and J. M. Chomaz, Experimental evidence for a new instability of a vertical columnar vortex pair in a strongly stratified fluid, *J. Fluid Mech.* **418**, 167 (2000).
- [26] H. P. Greenspan, *The Theory of Rotating Fluids* (Breukelen, New York, 1990).
- [27] P. G. Saffman, *Vortex Dynamics* (Cambridge University Press, Cambridge, 1992).
- [28] W. Thomson, Vibrations of a columnar vortex, *Philos. Mag.* **10**, 155 (1880).
- [29] J. J. Kobine, Inertial wave dynamics in a rotating and precessing cylinder, *J. Fluid Mech.* **303**, 233 (1995).
- [30] R. Lagrange, P. Meunier, F. Nadal, and C. Eloy, Precessional instability of a fluid cylinder, *J. Fluid Mech.* **666**, 104 (2011).
- [31] R. Manasseh, Breakdown regimes of inertia waves in a precessing cylinder, *J. Fluid Mech.* **243**, 261 (1992).
- [32] A. D. McEwan, Inertial oscillations in a rotating fluid cylinder, *J. Fluid Mech.* **40**, 603 (1970).
- [33] A. Mashayek and W. R. Peltier, The ‘zoo’ of secondary instabilities precursory to stratified shear flow transition. Part 1 Shear aligned convection, pairing, and braid instabilities, *J. Fluid Mech.* **708**, 5 (2012).
- [34] A. Mashayek and W. R. Peltier, The ‘zoo’ of secondary instabilities precursory to stratified shear flow transition. Part 2 The influence of stratification, *J. Fluid Mech.* **708**, 45 (2012).
- [35] A. Mashayek, C. P. Caulfield, and W. R. Peltier, Role of overturns in optimal mixing in stratified mixing layers, *J. Fluid Mech.* **826**, 522 (2017).
- [36] Y. Hattori and Y. Fukumoto, Modal stability analysis of a helical vortex tube with axial flow, *J. Fluid Mech.* **738**, 222 (2014).
- [37] O. M Phillips, On the dynamics of unsteady gravity waves of finite amplitude. Part I. The elementary interactions, *J. Fluid Mech.* **9**, 193 (1960).